

# UC Berkeley

## UC Berkeley Previously Published Works

### Title

An energy-optimized collimator design for a CZT-based SPECT camera

### Permalink

<https://escholarship.org/uc/item/54b5m6rk>

### Authors

Weng, Fenghua  
Bagchi, Srijeeta  
Zan, Yunlong  
[et al.](#)

### Publication Date

2016

### DOI

10.1016/j.nima.2015.09.115

Peer reviewed



Published in final edited form as:

*Nucl Instrum Methods Phys Res A*. 2016 January 11; 806: 330–339. doi:10.1016/j.nima.2015.09.115.

## An energy-optimized collimator design for a CZT-based SPECT camera

Fenghua Weng<sup>a</sup>, Srijeeta Bagchi<sup>b</sup>, Yunlong Zan<sup>a</sup>, Qiu Huang<sup>a,\*</sup>, and Youngho Seo<sup>b,c,\*</sup>

<sup>a</sup>School of Biomedical Engineering, Shanghai Jiao Tong University, Shanghai, China

<sup>b</sup>Physics Research Laboratory, Department of Radiology and Biomedical Imaging, University of California, San Francisco, CA, USA

<sup>c</sup>Department of Radiation Oncology, University of California, San Francisco, CA, USA

### Abstract

In single photon emission computed tomography, it is a challenging task to maintain reasonable performance using only one specific collimator for radio-tracers over a broad spectrum of diagnostic photon energies, since photon scatter and penetration in a collimator differ with the photon energy. Frequent collimator exchanges are inevitable in daily clinical SPECT imaging, which hinders throughput while subjecting the camera to operational errors and damage. Our objective is to design a collimator, which independent of the photon energy performs reasonably well for commonly used radiotracers with low- to medium-energy levels of gamma emissions. Using the Geant4 simulation toolkit, we simulated and evaluated a parallel-hole collimator mounted to a CZT detector. With the pixel-geometry-matching collimation, the pitch of the collimator hole was fixed to match the pixel size of the CZT detector throughout this work. Four variables, hole shape, hole length, hole radius/width and the source-to-collimator distance were carefully studied. Scatter and penetration of the collimator, sensitivity and spatial resolution of the system were assessed for four radionuclides including <sup>57</sup>Co, <sup>99m</sup>Tc, <sup>123</sup>I and <sup>111</sup>In, with respect to the aforementioned four variables. An optimal collimator was then decided upon such that it maximized the total relative sensitivity (*TRS*) for the four considered radionuclides while other performance parameters, such as scatter, penetration and spatial resolution, were benchmarked to prevalent commercial scanners and collimators. Digital phantom studies were also performed to validate the system with the optimal square-hole collimator (23 mm hole length, 1.28 mm hole width, 0.32 mm septal thickness) in terms of contrast, contrast-to-noise ratio and recovery ratio. This study demonstrates promise of our proposed energy-optimized collimator to be used in a CZT-based gamma camera, with comparable or even better imaging performance versus commercial collimators such as low-energy high resolution (LEHR) and medium energy general purpose (MEGP) collimators.

### Keywords

SPECT; CZT detector; collimator design; Monte Carlo simulation

---

\*Corresponding authors qiu Huang@sjtu.edu.cn, Tel:+86 21 62933086, Fax:+86 21 62933086, Zip: 200030 (Qiu Huang), youngho.seo@ucsf.edu (Youngho Seo).

## 1. Introduction

Single photon emission computed tomography (SPECT) radiotracers emit photons over a range of energies and collimator specifications vary with the energy levels of the radionuclides being imaged. Hence multiple collimators are required for imaging such as commercially available low-energy high-resolution (LEHR) and medium-energy general-purpose (MEGP) collimators coupled with conventional NaI(Tl) detectors[1]. This necessitates collimator exchanges between scans, sometimes even multiple times during the same day, and therefore hampers an efficient management of clinical imaging due to the time-consuming procedures. More importantly, low energy collimators generally are quite fragile, and their thin septa can be damaged easily by mechanical abuse (dropping, stacking on sharp objects, etc.).

Although, collimators are crucial for producing high quality tomographic images, they introduce artifacts into images from photons penetrating through the collimators and decreases sensitivity by absorbing/scattering photons. Thus, a careful collimator design with various criteria is essential in a new SPECT system to improve image quality[2]. The aim of this work, subsequently, has been to design a single collimator with improved sensitivity while maintaining comparable resolution over a broad spectrum of diagnostic energy levels.

The collimated gamma rays are traditionally detected by a scintillator coupled with photomultiplier tubes, which is still largely used in *in vivo* and non-invasive cross-sectional nuclear imaging. A renewed effort is being made to improve the quality of SPECT images by replacing these conventional indirect-conversion detectors with direct-conversion semiconductor detectors with better energy resolution[3][4]. Recent advances in fabricating solid-state detectors such as cadmium zinc telluride (CZT)[4][5] together with optimization of collimator designs[6][7][8] promise improvement in resolution and sensitivity of the front-end system. To that end, our energy-optimized collimator has been designed for a SPECT scanner equipped with a pair of relatively large-area CZT detectors with a small pixel pitch to operate over a broad range of gamma emission energies without collimator changes.

For a pixelated detector, a straightforward approach for maximizing sensitivity is to match the collimator holes with detector pixels to obtain a pixel-geometry-matching collimator (PGMC)[9][10]. Detectors combined with PGM-Cs are expected to be more efficient than non-pixel-matching collimations. The length, size, and shape of collimator holes, however, remain to be optimized to achieve energy independence. Researchers have proven that the extended low-energy general-purpose collimator (ELEGP) is a better choice than the MEGP collimator for mid-energy photons emitted from radiotracers such as  $^{111}\text{In}$  and  $^{123}\text{I}$ [11]. It was also found that the best performance could be obtained from a collimator that allowed a moderate amount of septal scatter and penetration[11][12]. Improved reconstruction algorithms also help compensate for the serious scattering and penetration[13]. New camera architecture[6] has sought to trade-off spatial resolution and sensitivity with pixelated semiconductor detectors. However, the majority of these papers have focused only on a specific radionuclide. Other efforts have been limited to optimizing collimators for simultaneous or sequential dual-isotope imaging[14][15]. There has been no initiative so far

to actually get rid of the energy dependency of SPECT nuclides on collimators by exploiting the superior energy resolution and high stopping power of CZT or CdTe detectors to avoid collimator changes.

In this paper, we describe the design characteristics of an optimized parallel-hole PGMC for a SPECT gamma camera using a CZT detector based on the Geant4 Monte Carlo simulations. Materials used are introduced with details on the tools adopted for evaluation, followed by the performance of the designed collimator combined with the large-area CZT detector. Our goal is to maximize sensitivity for acceptable values of other indices at low and medium energy gamma emissions from  $^{99m}\text{Tc}$ ,  $^{57}\text{Co}$ ,  $^{123}\text{I}$  and  $^{111}\text{In}$  radionuclides. Digital phantom studies are performed to validate the optimized energy-optimized collimator.

## 2. Materials and Methods

### 2.1. Collimator-detector model

In order to achieve improved image quality for an energy-optimized SPECT scanner, we use a relatively large-detection-area CZT-based detector ( $20.48 \times 20.48 \text{ cm}^2$ ) with a thickness of 5 mm (thinner than the typical NaI crystal of 3/8 inches thickness used for SPECT imaging) and a small pixel pitch of 1.60 mm. This CZT detector has been fabricated at Redlen Technologies, Canada with the electronics currently being designed at Brookhaven National Laboratory. The detector comprises  $8 \times 8$  modules of the  $16 \times 16$  arrays for a total of  $128 \times 128$  detector pixels.

When mounted to the CZT detector, collimators are designed such that the center of each collimator hole coincides with that of each detector pixel, hence the name pixel-geometry-matching collimator (PGMC). In other words, the pitch of the collimator hole is also set to be 1.60 mm. This pixel-matching collimation for a pixelated CZT detector gives high detection efficiency since the dead space on CZT resulting from collimator septa is small[16]. The designed collimator will be fabricated from high-density tungsten alloy (made of 91% tungsten, 6% nickel and 3% iron with a density of 17.1 – 17.3 g/cc), decreasing the rate of penetration in comparison to lead-based ones, with lower manufacturing costs than pure tungsten collimators.

The SPECT system model comprises of two opposing gamma cameras with compact CZT detectors and PGMCs. The model for the proposed SPECT system for different collimator hole shapes is shown in Figure 1.

### 2.2. Monte Carlo simulation

Geant4[17], one of the most advanced and supported toolkits in nuclear medical and particle physics, was employed here to fully simulate the CZT detectors and the parallel-hole collimators. Propagation of the particles in our simulations was dictated by the Low Energy Electromagnetic Physics list, with Livermore as the chosen physics model which has a validated energy range of 250 eV-100 GeV. The physics processes considered here include photoelectric effect, Compton scattering and Rayleigh scattering. The detector was set to be sensitive to all of the emitted particles to obtain detailed information about the interactions.

The Geant4 application developed was partly validated by comparing the simulated half-life times, main gamma energy peaks and emission possibilities of the four radionuclides used in our study with their respective theoretical values. The analytical values for resolution and sensitivity for a parallel square-hole collimator[18] were also calculated to verify the numerical values recorded from Geant4 with a similar design.

### 2.3. Iterative reconstruction

In-house codes for a maximum-likelihood expectation maximization (M-LEM) reconstruction algorithm were applied to reconstruct the simulated projection data, acquired with digital phantoms centered on the axis of rotation with a circular orbit at 120 equally spaced angular intervals from 0 to 360 degrees. Attenuation coefficients were calculated at the windowed-effective energy of each radionuclide. For  $^{111}\text{In}$ , the weighted average of the attenuation map based on the emission probabilities and linear attenuation coefficients were used[19]. Corrections for collimator and detector response and attenuation have been considered, but not for penetration and partial volume effects (PVE). The matrix size of the iteratively reconstructed images was  $128 \times 128 \times 128$  and the voxel size was  $1.6 \times 1.6 \times 1.6 \text{ mm}^3$ .

### 2.4. Performance estimation

With the simulated data from four radionuclides, scatter and penetration of the collimator, and sensitivity and spatial resolution of the system were thoroughly investigated. An 16% symmetrical energy window centered at the photo-peak energies 122 keV, 140.5 keV, 159 keV for  $^{57}\text{Co}$ ,  $^{99m}\text{Tc}$ ,  $^{123}\text{I}$  respectively and two 8% windows at 171 keV and 245 keV for  $^{111}\text{In}$ , were set to reject the scattering particles, assuring that at least half of the unnecessary particles were eliminated[20]. During each simulation,  $5 \times 10^6$  gamma rays were emitted in air from a point source placed at a distance of 10 cm from the collimator surface. Four simulations were performed for every experiment to reduce random errors.

The scattering rate and the penetration rate are both calculated for the gamma rays detected within the energy window. The former is estimated as the fraction of scattered photons (having at least one interaction with the collimator), while the latter is the portion penetrating through one or more septa without changing the incident direction. Sensitivity of the system is defined as the fraction of detected particles within the energy window among all the photons emitted, while the spatial resolution is measured as the full width at half maximum (FWHM) of a point-spread function (PSF), fitted by a symmetric Gaussian function.

### 2.5. Collimator optimization

The collimator performance, and accordingly the performance of the detector and imaging system, varies with the imaging radiotracers due to the different energy levels of the photons they emit. Thus the desired collimator dimensions for different radiotracers cannot be the same. The rationale adopted for optimizing an energy-optimized collimator is to maximize the total relative sensitivity (*TRS*) for the four considered radionuclides while maintaining other performance parameters (including spatial resolution, penetration and so on) comparable to those obtained with the commercial ones such as LEHR/ MEGP collimators.

Based on collimator scatter, penetration, system resolution and sensitivity evaluated for different radionuclides, we determined permissible ranges for geometrical parameters of the collimator and optimized the collimator within these permissible ranges via the total relative sensitivity. For a given radioactive nuclide and a given collimator, the relative sensitivity is defined as the sensitivity obtained with this specific collimator divided by the maximum sensitivity that can be achieved by any collimator in the permissible ranges. Assuming equal weight for the considered radionuclides, for a given collimator, the total relative sensitivity is defined as the sum of four relative sensitivities:

$$TRS = \sum_{i=1}^4 \frac{S^i}{S_{max}^i}. \quad (1)$$

In Equation 1,  $S^i$  denotes the sensitivity of the  $i$ th radionuclide and  $S_{max}^i$  is the maximal sensitivity obtained with the  $i$ th radionuclide. The optimal collimator is chosen as

$$TRS_{opt} = \operatorname{argmax}(TRS). \quad (2)$$

## 2.6. System validation

The SPECT imaging system equipped with the optimal collimator is validated using digital phantoms in terms of the contrast, contrast-to-noise ratio and recovery ratio.

Contrast, a quantitative measurement of the differences in intensity of the reconstructed image, was evaluated using a hot phantom. The hot phantom shown in Figure 2 (a) consists of six radioactive hot rods. The rods with different sizes ranging from 9.6 mm to 17.6 mm in radii are placed in a non-radioactive water-filled cylinder with a diameter of 16 cm and height 2 cm, and filled with aqueous solutions of  $^{57}\text{Co}$ -/ $^{99m}\text{Tc}$ -/ $^{123}\text{I}$ -/ $^{111}\text{In}$ - sodium pertechnetates at a concentration of 60 kBq/ml. Contrast denoted by  $C$  is given by

$$C = \frac{M_{ROD} - M_{BG}}{M_{ROD} + M_{BG}} \times 100\%, \quad (3)$$

where,  $M_{ROD}$  is the average activity in each of the six hot rod regions and  $M_{BG}$  is the average activity in the background ROI (the circle with red dashed line centered in the phantom) containing 1961 pixels for each slice. To reduce the statistical variations, 6 sequential slices selected from the middle of the rods were averaged. The corresponding contrast-to-noise ratio ( $CNR$ ) is defined as

$$CNR = \frac{M_{ROD} - M_{BG}}{NSD}, \quad (4)$$

where  $NSD$  is the standard deviation of the uniform background ROI.

One potential application of a gamma system with the proposed energy-optimized collimator and the CZT detector is in brain imaging. Thus a DaT (dopamine transporters) SPECT imaging study was simulated here using a striatal phantom filled with  $^{99m}\text{Tc}$  or  $^{123}\text{I}$  solution and the recovery ratios were recorded. As a target organ, the left striatal compartment (left

caudate nucleus and left putamen) and right striatal compartment (right nucleus and right putamen) were separated from the background based on a segmented magnetic resonance image. Different intensities of radioactive solutions with different striatal-to-background uptake ratios, ranging from 3:1 to 10:1 were set and simulated. One slice of the five-compartment brain striatal phantom with the different activity levels is shown in Figure 2 (b) and the recovery ratio  $Rr$  is estimated by the following equation

$$Rr = \frac{(M_{STRILATAL}/M_{BG})_{Measured}}{(M_{STRILATAL}/M_{BG})_{Real}}, \quad (5)$$

where  $M_{STRILATAL}$  is the mean value of the left/right striatal region and  $M_{BG}$  is the mean value of the background (the circle with red dashed line in Figure 2 (b)).

### 3. Results

We first illustrate the simulation results of four figures of merit (the collimator scatter and penetration, system sensitivity and resolution) for four radionuclides ( $^{57}\text{Co}$ ,  $^{99m}\text{Tc}$ ,  $^{123}\text{I}$  and  $^{111}\text{In}$ ) with respect to four variables (hole length, radius, source-to-collimator distance and hole shape). In each simulation, one variable varied while the other three stayed unchanged. If not specified otherwise, a square hole collimator with a bore thickness of 24 mm and radius 0.65 mm was used with the radionuclide located 10 cm away from the collimator surface.

#### 3.1. Scatter and penetration

Among all the four nuclides, nuclide  $^{99m}\text{Tc}$  emitted the smallest percentage of scattered photons as shown in the left column of Figure 3, owing to its pure mono-emission at 140.5 keV. As compared to  $^{99m}\text{Tc}$  at 140.5 keV, more scattered photons were detected in the 122 keV energy window of  $^{57}\text{Co}$ , because besides the 122 keV photons,  $^{57}\text{Co}$  produces 136 keV photons as well, some of which down-scatter to the energy window of the 122 keV photo peak.  $^{111}\text{In}$ , not surprisingly, has the highest scattering rate and the highest penetration rate.

The rates of the penetrated and scattered gamma rays both decrease as the hole length increases shown in Figures 3 (a) and (b). When the hole length is less than 21 mm, for  $^{111}\text{In}$ , penetration and scatter together account for over 60%. If less deterioration is expected, a collimator with square holes (radius being 0.65 mm) should be longer than 21 mm. Similarly from Figures 3 (c) and (d), we find that a square-hole collimator with a hole length of 24 mm should have a radius smaller than 0.66 mm to ensure the total scatter and penetration is less than 60%.

When increasing the distance from the source to the collimator surface, it is clear that the scattering rate declines as depicted in Figure 3 (e), however, the penetration component increases as shown in Figure 3 (f), no matter which radioisotope is simulated. The total proportion of scatter and penetration decreases as the distance increases for  $^{111}\text{In}$ , but stays stable for  $^{57}\text{Co}$ ,  $^{99m}\text{Tc}$  and  $^{123}\text{I}$  beyond 16 cm.

As for the bore shape graphs shown in Figures 3 (g) and (h), the collimator with square holes yields the highest fraction of unwanted particles. However the degradation is not so obvious as to counteract the higher sensitivity resulting from the square hole collimator, as illustrated in the next subsection.

It can be seen from the subplots in Figure 3 that obvious variations exist in scattering and penetration for high energy photon emitters. Thus rigorous comparison endeavors are necessary especially for  $^{111}\text{In}$ . In the following context, for a fair comparison, only half of the sensitivity for  $^{111}\text{In}$  was calculated unlike the three other radionuclides, since  $^{111}\text{In}$  emits two photons (171 keV and 245 keV) with almost equal emission probabilities (90% and 94%).

### 3.2. Resolution and sensitivity

Figure 4 (a) shows that the system resolution is the best when imaging  $^{57}\text{Co}$  point source and the worst for  $^{111}\text{In}$  imaging, with a square hole (0.65 mm radius) collimator. For sensitivity variation shown in Figure 4 (b),  $^{111}\text{In}$  yields the highest among the four nuclides when the hole length is less than 22 mm, however, as the hole length increases, the detection efficiency with  $^{57}\text{Co}$  surpasses half of that with  $^{111}\text{In}$ . Relatively, the detector shows the least sensitivity with  $^{123}\text{I}$ .

The deflation of spatial resolution (Figure 4 (c)) and the amplification of detection efficiency (Figure 4 (d)) as the bore radius changes from 0.62 mm to 0.67 mm are also illustrated when the hole length is 24 mm. The sensitivity for  $^{111}\text{In}$  is higher than that for the three other radionuclides when hole radius is larger than 0.66 mm, although the difference in resolution is small. This is observed because the penetration is more severe and scatter non-negligible, as the septa get thinner. The interval in hole radius of 0.01 mm effectively changes the diameter by 0.02 mm.  $^{111}\text{In}$  quickly increases penetration in comparison to low-energy tracers making this range crucial for optimizing performance.

As expected, the distance from the collimator surface strongly affects the collimator resolution (Figure 4 (e)). Taking  $^{99m}\text{Tc}$  as an example, the amplification is over 150% when the distance changes from 7 cm to 10 cm. The sensitivities of the nuclides in Figure 4 (f) stay nearly unchanged except for  $^{111}\text{In}$  because of the existence of a larger proportion of penetrated and scattered particles.

Figures 4 (g) and (h) show the results of the four radionuclides using a PGMC with various hole shapes. Using  $^{111}\text{In}$  to illustrate the trend noted, square holes provided 9.84% worse spatial resolution while giving 108.43% higher sensitivity than circular holes, and 5.15% lower spatial resolution but an increase of 43.81% in sensitivity than hexagonal holes on average. The results show that square bore is superior to the other two types of bores in terms of obtaining higher sensitivity with insignificant degradation in resolution.

In general, the collimator parameters affect the sensitivity for  $^{111}\text{In}$  more than they do for the three other radionuclides (Figure 4), due to the larger variation they cause in scattering and penetration for  $^{111}\text{In}$  (Figure 3).



### 3.3. Optimized collimator design via TRS maximization

Based on collimator scatter, penetration, system resolution and sensitivity evaluated for different radionuclides, we determined permissible ranges for geometrical parameters of the collimator. The results from varying hole length at four energy levels yielded the optimum range to be between 23–25 mm. Similarly, we varied the hole radius and observed acceptable performance between 0.63–0.65 mm. Three source-to-collimator distances indicated as short (4 cm), medium (13 cm) and long (22 cm) were simulated for different applications. The behaviors of the three hole shapes presented in Figures 4 (g) and (h) show that square holes give much higher sensitivity at the cost of a slight decline in resolution for all radionuclides tested when compared to hexagonal and circular holes. Higher sensitivity is very essential to better image qualities[6]. Hence, the square-hole collimator was our primary step towards gaining a better detection efficiency.

With the permissible ranges for geometrical parameters of the collimator, the total relative sensitivity was calculated as in Equation 1, where the maximum sensitivity in the permissible ranges is 337, 302, 281 and 612 cpm/uCi for  $^{57}\text{Co}$ ,  $^{99m}\text{Tc}$ ,  $^{123}\text{I}$  and  $^{111}\text{In}$ , respectively. The *TRS* calculated for the square-hole collimators when the source-to-collimator surface distance is 13 cm was listed in Table 1, together with the sensitivity for each radionuclide.

The highest *TRS* value is obtained when the hole radius is 0.65 mm and the hole length is 23 mm as deduced from Table 1. Similar trends in results are observed for both short and large distances. However, the total scattering and penetration rate is about 57% (over 50%) with  $^{111}\text{In}$  for the short distance. Thus, the one with the second highest *TRS* value and 49.79% of total scattering and penetration rate is regarded as the optimum configuration for our project, namely, the tungsten-alloy-based collimator with square holes having a radius of 0.64 mm and hole length of 23 mm. Compared to the one with the highest *TRS* value, the optimum collimator provides a 7.15% decrease in scattering rate and a 12.57% decrease in penetration rate, with a 3.32% improvement in resolution for  $^{111}\text{In}$  when the source-to-collimator distance is 4 cm.

### 3.4. Validation

**3.4.1. Contrast and CNR**—To evaluate the performance of the proposed optimum PGMC, simulated projection data from the hot rod phantom were acquired over 30 minutes for a total of 120 projection angles for contrast studies. The distance from the phantom center to the collimator surface was set to be 13 cm. The images reconstructed with 30 iterations for four radionuclides are presented in Figure 5 and the line profiles across the hot rods with radii of 11.2 mm as well as 17.6 mm were also plotted. The contrast and *CNR* for the six hot rod radii and four radionuclides are shown in Figure 6.

Obviously, the image for  $^{57}\text{Co}$  has the largest *CNR* value as well as the best contrast over the three other radionuclides from Figure 6, which was expected since the septa absorb photons with lower energy more effectively leading to a lower level of septal penetration. Although the contrast of  $^{111}\text{In}$  is better, the *CNR* is poorer than that of  $^{123}\text{I}$ , due to the higher noise level of  $^{111}\text{In}$ . However, the lowest contrast is still over 90% and *CNR* is over 15, indicating

the good ability of the system to distinguish different levels of activities. The image quality of  $^{111}\text{In}$  is preserved owing to the high sensitivity even with a higher proportion of penetrated photons.

**3.4.2. Recovery ratio**—Two simulations were also performed to evaluate the recovery ratio of the PGMC. Each was conducted for  $^{123}\text{I}$  and  $^{99\text{m}}\text{Tc}$  separately. In the first simulation, the left and right striatal regions were filled with radionuclides with striatal to background activity ratios of 6:1 and 3:1, respectively. While in the second acquisition, striatum-to-background ratios were set to be 10:1 (left) and 8:1 (right). The recovery ratios from the reconstructed images after 45 iterations were measured and tabulated in Table 2. The striatal and background ROIs were drawn after reconstruction by multiplying a mask based on the original striatal phantom.

The recovery ratios listed in Table 2 for  $^{99\text{m}}\text{Tc}$  and  $^{123}\text{I}$  are both comparable with some other published results. The images for  $^{99\text{m}}\text{Tc}$  provide better recovery than that for  $^{123}\text{I}$  due to less scatter and penetration. However, the measured ratio over real ratio decreases as the real ratio increases due to the larger PVE. It has been reported that over 50% of the radioactivity concentration in the striatum was underestimated since the background with lower activity was overestimated due to the effect of spillover from adjacent striatal regions with higher activities. The capability to recover activity concentration ratios for this system can be further improved if the PVE is applied in the reconstruction algorithm[21].

### 3.5. Benchmarking the optimized design with existing collimators

Established by the *TRS* analysis, as well as contrast and recovery evaluation described above, we finally list the dimensions for the optimum collimator configuration in Table 3 and compare its performance with the BiCore™ collimators.

Compared to the conventional Siemens LEHR and MELP (medium energy low penetration) collimators, the proposed optimal energy-optimized collimator has comparable sensitivity, more septal penetration, and higher resolution as shown in the last three rows in Table 3. Taking  $^{99\text{m}}\text{Tc}$  imaging as an example, there is about a 6.62% improvement in resolution and a 29.20% increment in detection efficiency compared to the LEHR collimator. In addition, the resolution and sensitivity of the proposed collimator configuration are contrasted to those in other studies[22], and to some commercial scanners. Though sensitivity and resolution values depend on the isotope, detector spatial resolution, crystal thickness and the gap between the collimator and crystal, the comparison in Table 4 highlights the potential of the energy-optimized CZT-based SPECT system to provide comparable or even better imaging quality.

## 4. Discussion

In this study, various designs of the parallel-hole collimators have been compared for different radiotracers emitting energies below 250 keV. The performance of the large-area CZT-based detector combined with the PGMC has been studied to establish the possibility of fabricating an energy-optimized SPECT system. The quality of the gamma-camera system designed to image small targeted volumes at low- and medium-energy ranges was

quantitatively assessed by utilizing two voxel-based phantoms. The results have shown that, with an appropriate design of the PGMC, it is possible to obtain comparable or even better images using four different radionuclides ( $^{57}\text{Co}$ ,  $^{99m}\text{Tc}$ ,  $^{123}\text{I}$  and  $^{111}\text{In}$ ) without collimator exchanges, compared to image qualities acquired using the conventional SPECT system with commercial collimators such as LEHR and MEGP ones.

The strength of this work lies in the compromised design for imaging four radionuclides simultaneously based on the total relative sensitivity. We had to sacrifice the performance for nuclides emitting low energy photons to reduce the scatter and penetration for  $^{111}\text{In}$ . Fortunately, the sensitivity for  $^{111}\text{In}$  is high and it has been reported that a better imaging performance of  $^{111}\text{In}$  can be obtained from a collimator that allows a certain fraction of penetrated and scattered particles[12]. Another way to compensate for the two pollution effects is to develop a more accurate reconstruction method[11].

The collimator proposed was designed for direct-conversion pixelated CZT detectors, which offer higher stopping power and better pixel isolation at the same thickness than conventional indirect-conversion scintillation detectors, such as those using the NaI(Tl) crystal, hence obtaining considerable sensitivity and adequate resolution even at high energy. The excellent energy resolution of the CZT detector allow us to acquire SPECT data using narrower energy windows (4% – 8%) filtering most of the unnecessary photons without obvious deterioration in detection efficiency.

Combined with the large-detection-area CZT detector, the parallel-hole PGM-C was designed to improve efficiency and decrease aliasing artifacts since the collimator holes directly overlap the detector pixels. To determine the optimal combination of the collimation and detection, various configurations of the collimators were investigated using sensitivity, resolution, scattering and penetration. The values presented in Figure 3 and Figure 4 guided us to decide reasonable ranges for different parameters. The parameter space for hole radius is limited to elucidate the rapid variation of penetration and sensitivity for  $^{111}\text{In}$  as evident from Figure 3 (d) and Figure 4 (d). The range chosen is crucial in optimizing the collimator since  $^{111}\text{In}$  quickly increases penetration here in comparison to low-energy tracers. Since the optimum dimension of the collimator differs with different radioisotopes, *TRS* was defined to comprehensively investigate the performance of the given radiopharmaceuticals. It is obvious that the sensitivity of  $^{111}\text{In}$  is much higher than that of the three other radiotracers. However, the penetrated and scattered photons are in fact the predominant contributors in producing high sensitivity for  $^{111}\text{In}$ .

Fortunately, it has been reported that a high sensitivity is desired in detecting small tumors, even when the images are not reconstructed from the correctly collimated photons alone[11]. The preferred collimator design for energy-independence was decided based on the *TRS* calculation. Contrast, mostly used to characterize the system performance[6][11][23] was calculated using the hot rod phantom with six rods to validate the preferred collimator design. Though the performances degraded at high energies, image contrast was preserved and *CNR* was shown to be consistent in Figure 6. Even for the hot rod with a radius of 9.6 mm, the contrast for  $^{111}\text{In}$  is over 90%, demonstrating the good ability of the system to distinguish different activity levels. An optimized energy window might offer some benefit

in further improving the image quality[23][24] . We will be following up the current study by investigating the effects of the energy window settings on the capability of the CZT-based system.

The SPECT camera presented in this work could find potential applications in imaging small-volume organs such as human brain, breast and prostate. One of the applications studied for brain imaging for early detection of Parkinsons disease was simulated using the striatal phantom. The recovery ratios for  $^{99m}\text{Tc}$  and  $^{123}\text{I}$  were enlisted in Table 2 at different striatum to background ratio settings. The values are comparable or even better though the penetration and PVE corrections have not yet been incorporated in the reconstructed algorithm compared with other results[25][26]. The compensations for penetration correction and PVE will be developed in following work to improve the reconstruction. Dual-isotope imaging will also be carried out to take advantage of the good energy resolution of the CZT detector.

Further investigation, however, is required to evaluate if the capability of the system to image at higher energies can be improved by using thicker or longer collimator holes such as in the four-pixel matching[10] and nine-pixel matching collimator designs[27] which will allow thicker septa and higher sensitivity. Experimental validations are still required in the near future as a proof-of-concept for preclinical trials.

## 5. Conclusion

The performances of the SPECT system for imaging four commonly used radionuclides emitting photons at low and medium energy levels were compared for various configurations of the PGMs. The behavior of the CZT-based detector in combination with PGMs was also studied. We found that the PGM made of tungsten-alloy with square holes of radius 0.64 mm and bore length of 23 mm is best suited for energy independence. Preliminary simulated results prove that with such an energy-optimized collimator, the SPECT system is feasible and promising, providing acceptable image quality for a variety of radionuclides to image small targeted volumes. The use of a single collimator for imaging radiotracers targeting different organs will minimize the risk of collimator damage from interchanging collimators, while enabling an efficient workflow.

## Acknowledgments

This work was supported in part by the National Institute of Health (NIH) under Grant No. R01EB012965, by the International Science & Technology Cooperation Program of China under Grant No. 2013DFB30270 and by the National Natural Science Foundation of China under Grant No. 81201114 & No. 91330102.

## References

1. Madsen MT. Recent advances in spect imaging. *The Journal of Nuclear Medicine*. 2007; 48(4):661–673. [PubMed: 17401106]
2. Moore SC, Kouris K, Cullum I. Collimator design for single photon emission tomography. *European Journal of Nuclear Medicine*. 1992; 19(2):138–150. [PubMed: 1563442]
3. Peterson TE, Furenlid LR. Spect detectors: the anger camera and beyond. *Physics in Medicine and Biology*. 2011; 56(17):145–182.

4. Iniewski K. Czt detector technology for medical imaging. *Journal of Instrumentation*. 2014; 9(1):C11001.
5. Wangerin K, Du YF, Jansen F. Czt performance for different anode pixel geometries and data corrections. *Nuclear Instruments and Methods in Physics Research Section A*. 2011; 648:S37–S41.
6. Robert C, Montemont G, Rebuffel V, Buvat I, Guerin L, Verger L. Simulation-based evaluation and optimization of a new cdznte gamma-camera architecture (hisens). *Physics in Medicine and Biology*. 2010; 55(9):2709–2726. [PubMed: 20400808]
7. Trinci G, Massari R, Scandellari M, Boccacini S, Costantini S, Sero RD, Basso A, Sala R, Scopinaro F, Soluri A. A new variable parallel holes collimator for scintigraphic device with validation method based on monte carlo simulations. *Nuclear Instruments and Methods in Physics Research Section A*. 2010; 621(1–3):406–412.
8. Watanabe K, Sugiyama J, Yamazaki A, Uritani A. Development of a gamma-camera with a functional collimator. *Nuclear Instruments and Methods in Physics Research Section A*. 2011; 652(1):582586.
9. Suzuki A, Takeuchi W, Ishitsu T, Tsuchiya K, Ueno Y, Kobashi K. A four-pixel matched collimator for high-sensitivity spect imaging. *Physics in Medicine and Biology*. 2013; 58(7):2199–2217. [PubMed: 23475193]
10. Suzuki A, Takeuchi W, Ishitsu T, Tsuchiya K, Morimoto Y, Ueno Y, Kobashi K, Kubo N, Shiga T, Tamaki N. High-sensitivity brain spect system using cadmium telluride (cdte) semiconductor detector and 4-pixel matched collimator. *Physics in Medicine and Biology*. 2013; 58(21):7715–7731. [PubMed: 24140804]
11. Mahler E, Sundstrom T, Axelsson J, Larsson A. Detecting small liver tumors with (111)in-pentetreotide spectra collimator study based on monte carlo simulations. *IEEE Transactions on Nuclear Science*. 2012; 59(1):47–53.
12. Lu Y, Chen L, Gindi G. Collimator performance evaluation for in-111 spect using a detection/localization task. *Physics in Medicine and Biology*. 2014; 59(3):679–696. [PubMed: 24442348]
13. He B, Du Y, Song X, Segars WP, Frey EC. A monte carlo and physical phantom evaluation of quantitative in-111 spect. *Physics in Medicine and Biology*. 2005; 50(17):4169–4185. [PubMed: 16177538]
14. Inoue Y, Shirouzu I, Machida T, Yoshizawa Y, Akita F, Minami M, Ohtomo K. Collimator choice in cardiac spect with i-123labeled tracers. *Journal of Nuclear Cardiology*. 2004; 11(4):433–439. [PubMed: 15295412]
15. De Geeter F, Franken P, Defrise M, Andries H, Saelens E, Bossuyt A. Optimal collimator choice for sequential iodine-123 and technetium-99m imaging. *Medical Physics*. 1996; 23(7):768–774.
16. Weinmann AL, Hruska CB, O'Connor MK. Design of optimal col-limation for dedicated molecular breast imaging systems. *Medical Physics*. 2009; 36(3):845–856. [PubMed: 19378745]
17. Allison J, et al. Geant4 Collaboration. Geant4 developments and applications. *IEEE Transactions on Nuclear Science*. 2006; 53(1):270–278.
18. Gunter DL. Collimator design for nuclear medicine. *Emission Tomography*. 2004:153–168.
19. Seo Y, Wong KH, Hasegawa BH. Calculation and validation of the use of effective attenuation coefficient for attenuation correction in in-111 spect. *Medical Physics*. 2005; 32(12):3628–3635. [PubMed: 16475761]
20. Parka S-J, Yu AR, Choi YY, Kim KM, Kim H-J. Optimal energy window selection of a czt-based small-animal spect for quantitative accuracy. *Nuclear Instruments and Methods in Physics Research Section A*. 2015; 782:104–111.
21. Erlandsson K, Thomas B, Dickson J, Hutton BF. Partial volume correction in spect reconstruction with osem. *Nuclear Instruments and Methods in Physics Research Section A*. 2011; 648:S85S88.
22. Zeinali HZ. Results of the measurement of the collimator hole angula-tion for different collimators of spect with adaptive quality control phantom. *Modern Instrumentation*. 2012; 1(4):49–53.
23. Campbell DL, Peterson TE. Simulation study comparing high-purity germanium and cadmium zinc telluride detectors for breast imaging. *Physics in Medicine and Biology*. 2014; 59(22):7059–7079. [PubMed: 25360792]

24. Park S-J, Yu AR, Choi YY, Kim KM, Kim H-J. Optimal energy window selection of a czr-based small-animal spect for quantitative accuracy. *Nuclear Instruments and Methods in Physics Research Section A*. 2015; 782:104111.
25. Kao PF, Wey SP, Yang AS. Simultaneous 99mTc and 123I dual-isotope brain striatal phantom single photon emission computed tomography: validation of 99mTc-trodat-1 and 123I-ibzm simultaneous dopamine system brain imaging. *The Kaohsiung journal of medical sciences*. 2009; 25(11):601–607. [PubMed: 19858039]
26. Vanzi E, De Cristofaro MT, Ramat S, Sotgia B, Mascalchi M, Formiconi AR. A direct ROI quantification method for inherent pve correction: accuracy assessment in striatal spect measurements. *European journal of nuclear medicine and molecular imaging*. 2007; 34(9):1480–1489. [PubMed: 17390134]
27. Suzuki A, Takeuchi W, Yuichiro Y, Ueno Morimoto, Kubo N, Shiga T, Tamaki N. Nine-pixel matched collimator for low- and medium-energy spect imaging (abstract). *Journal of Nuclear Medicine*. 2014; 55:2145.

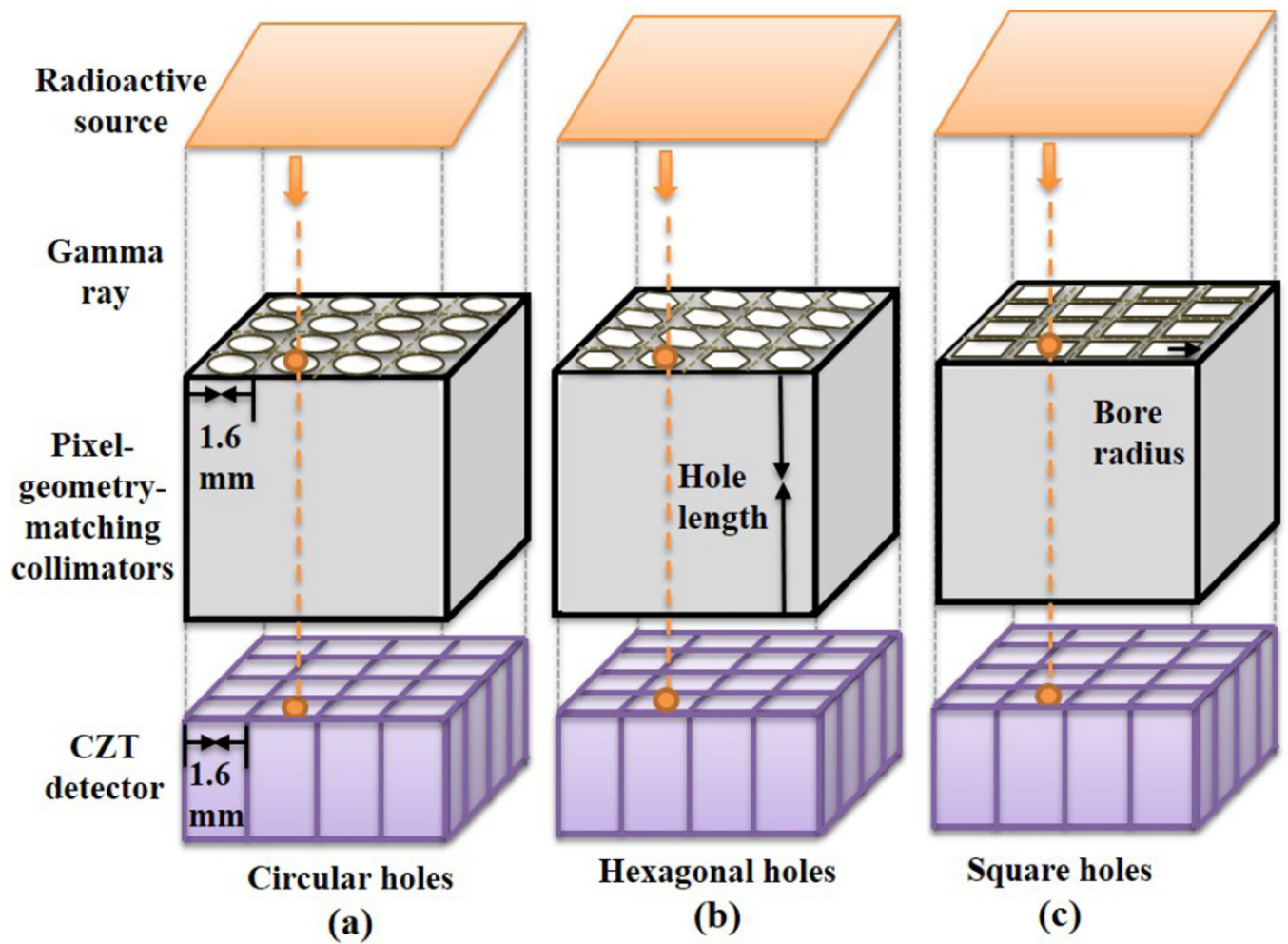


**Figure 1.** Model of the pixel-geometry-matching collimators with (a) circular holes, (b) hexagonal holes and (c) square holes mounted with CZT detectors.

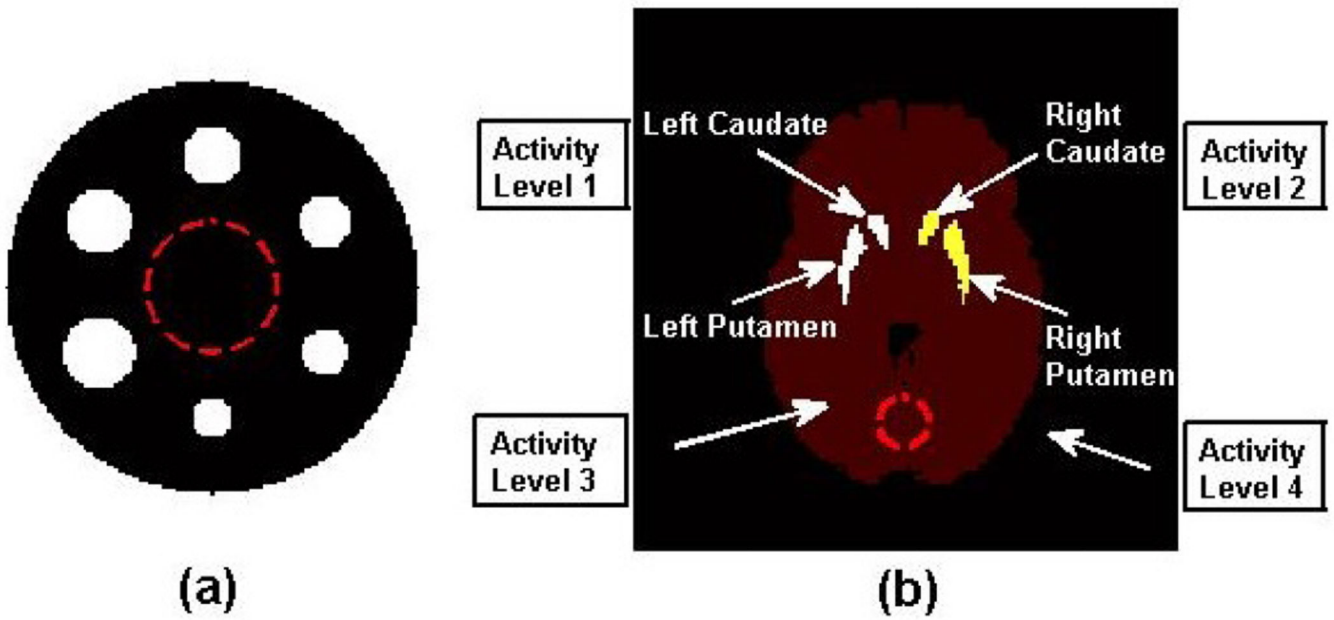


**Figure 2.**

(a) Diagram of the hot rod phantom: the rod radii are 9.6 mm, 11.2 mm, 12.8 mm, 14.4 mm, 16.0 mm and 17.6 mm with 1.6 mm interval. (b) A cross section of the five-compartment brain striatal phantom with the different activity levels used for recovery ratio studies, the striatal phantom has four levels of activities and the regions labeled by level 4 remained non-radioactive.



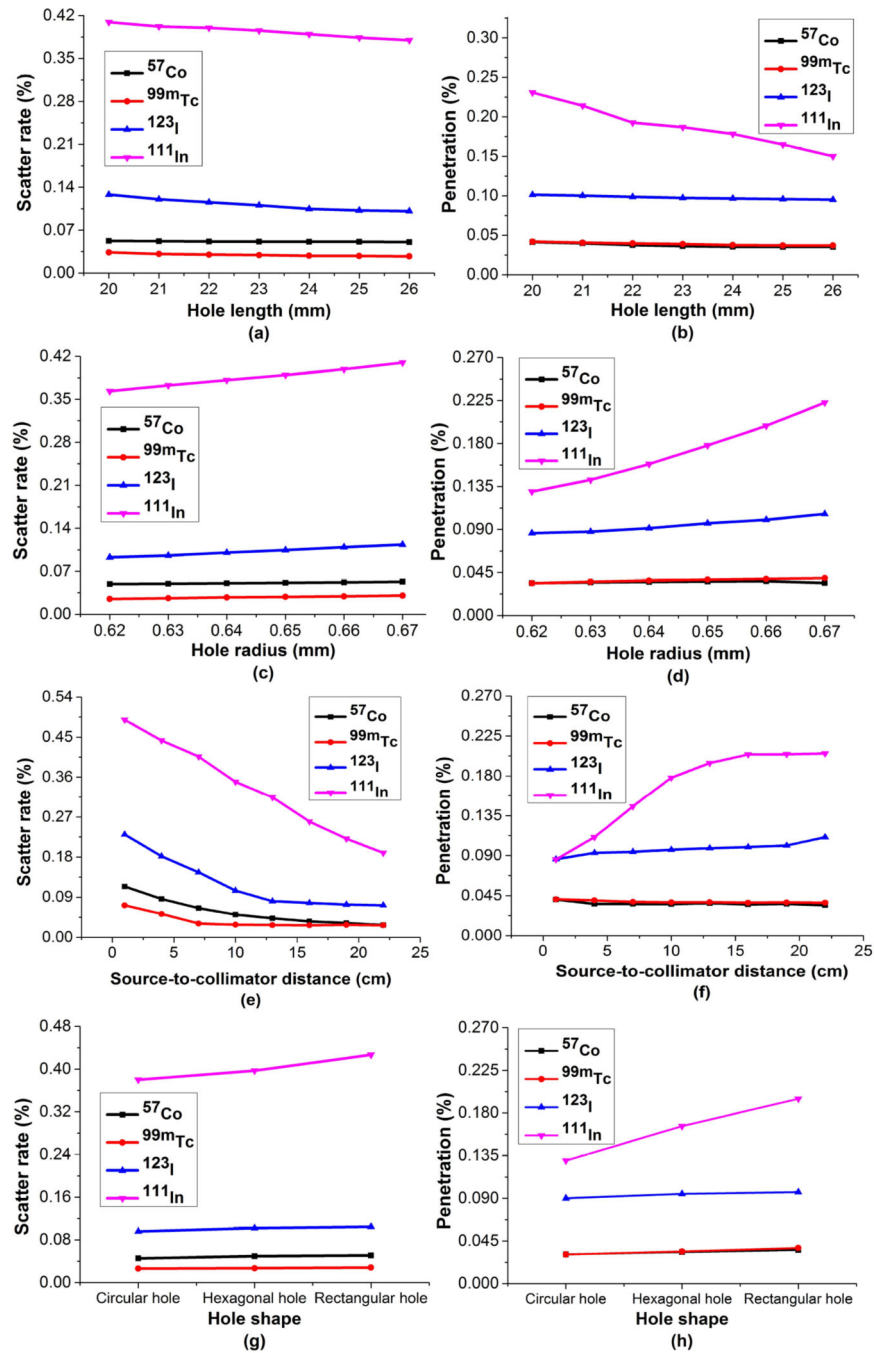


**Figure 3.**

The scattering (left column) and penetration (right column) components measured by changing (a)–(b) hole length, (c)–(d) hole radius, (e)–(f) source-to-collimator surface distance and (g)–(h) hole shape of the gamma system for  $^{57}\text{Co}$  radionuclide (black squares marked),  $^{99\text{m}}\text{Tc}$  radionuclide (red circles marked),  $^{123}\text{I}$  radionuclide (blue upper-triangles marked) and  $^{111}\text{In}$  radionuclide (cyan lower-triangles marked).

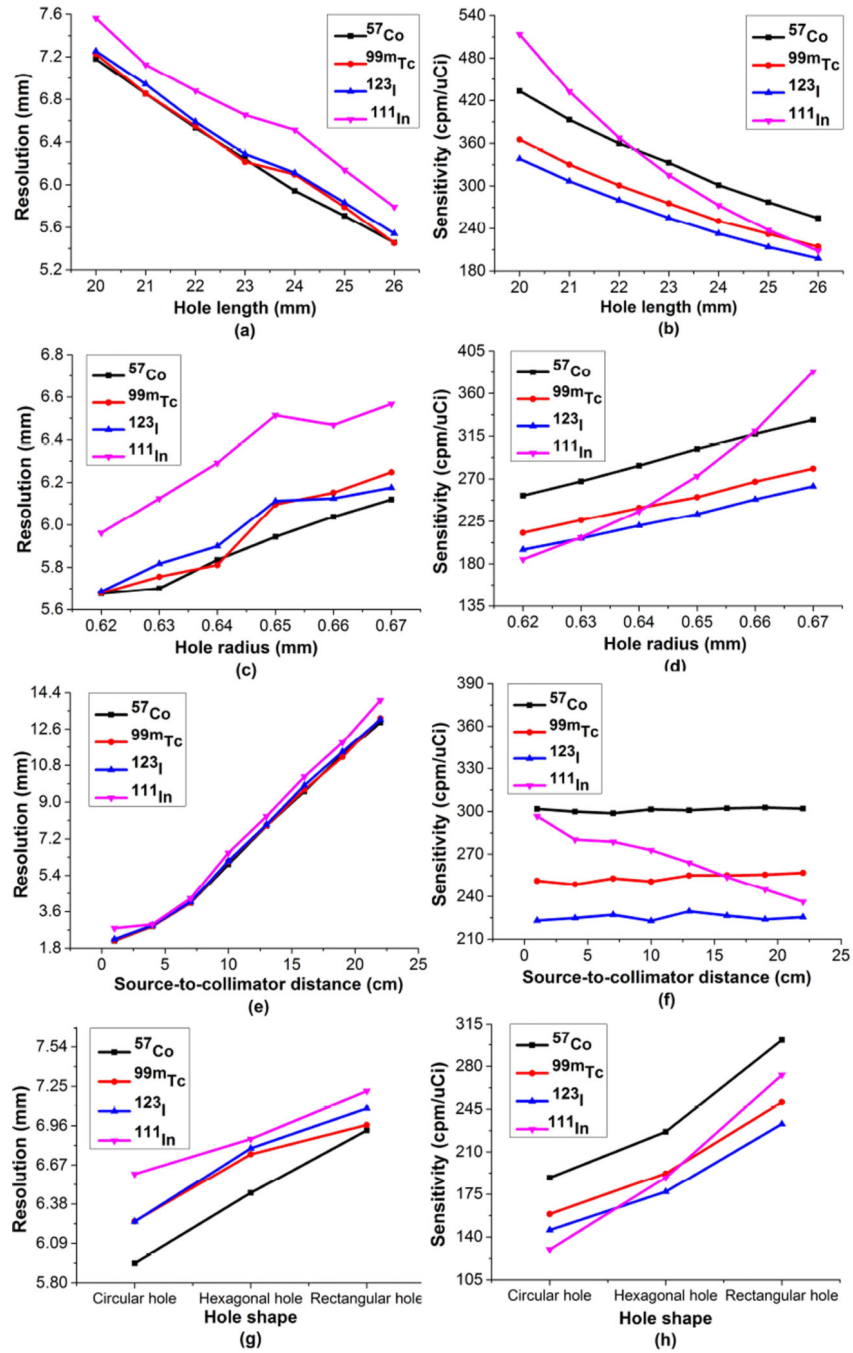


**Figure 4.** The resolution (left column) and sensitivity (right column) measured by changing (a)–(b) hole length, (c)–(d) hole radius, (e)–(f) source-to-collimator surface distance and (g)–(h) hole shape of the gamma system for  $^{57}\text{Co}$  radionuclide (black squares marked),  $^{99\text{m}}\text{Tc}$  radionuclide (red circles marked),  $^{123}\text{I}$  radionuclide (blue upper-triangles marked) and  $^{111}\text{In}$  radionuclide (cyan lower-triangles marked and only half of the sensitivity shown).

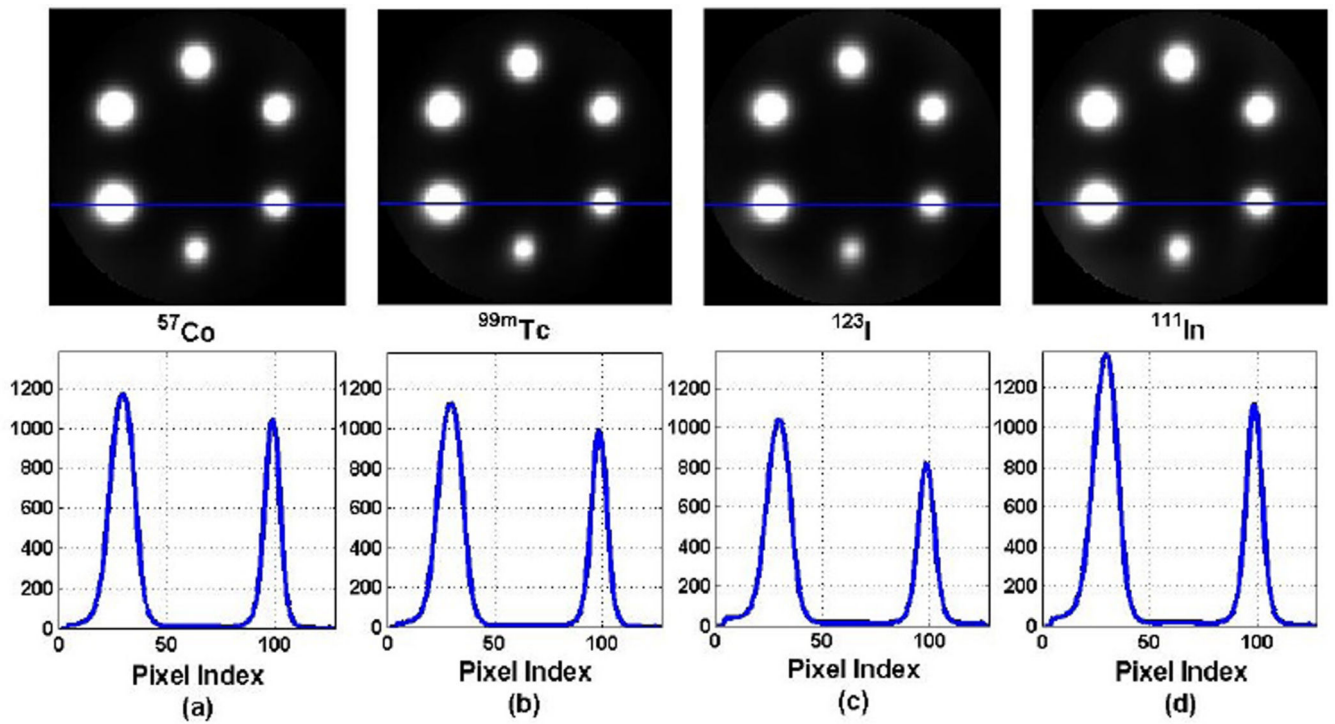


**Figure 5.**

Comparison of the reconstructed images with 30 iterations and the corresponding profiles across the hot rods with radii 11.2 mm and 17.6 mm on the lower half of the phantom for (a)  $^{57}\text{Co}$ , (b)  $^{99m}\text{Tc}$ , (c)  $^{123}\text{I}$  and (d)  $^{111}\text{In}$  radioisotopes.

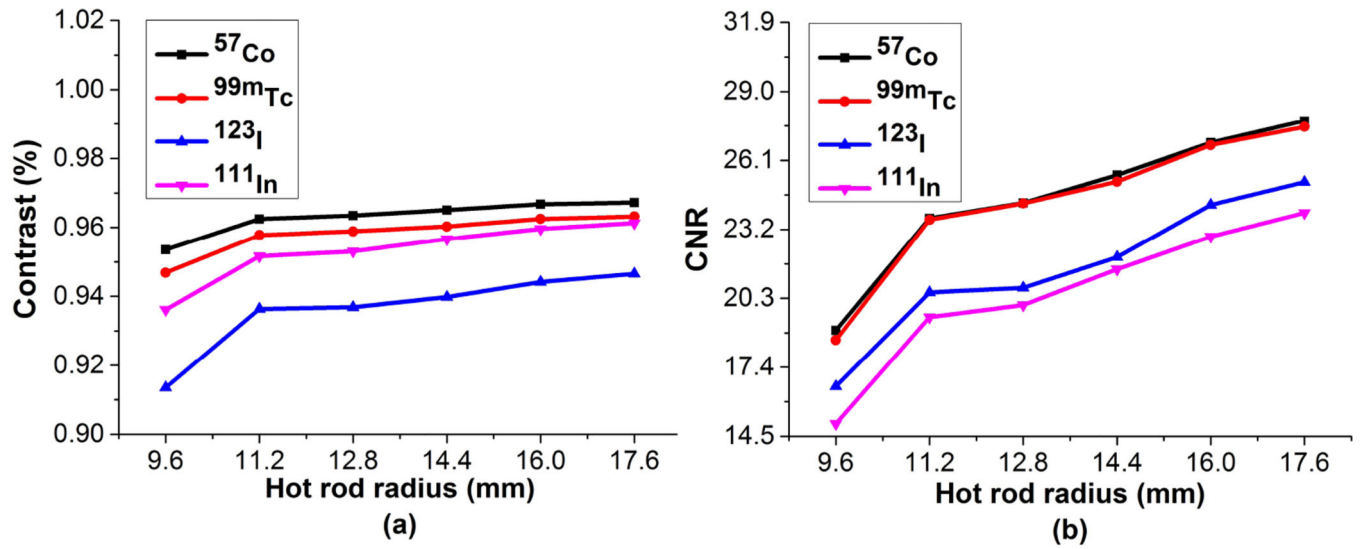


**Figure 6.**

Comparison of the (a) contrast and (b) CNR changing the rod radius for  $^{57}\text{Co}$  nuclide (black squares marked),  $^{99\text{m}}\text{Tc}$  (red circles marked),  $^{123}\text{I}$  (blue upper-triangles marked) and  $^{111}\text{In}$  radionuclides (cyan lower-triangles marked).

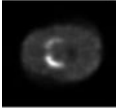
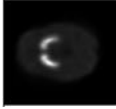
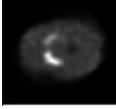

**Table 1**

*TRS* calculated for the square-hole collimators for the medium distance.

Hole length	Hole radius	Sensitivity (cpm/uCi)			<i>TRS</i>
		<sup>57</sup> Co	<sup>99m</sup> Tc	<sup>111</sup> In	
23 mm	0.63 mm	286	243	229	454
	0.64 mm	309	259	247	497
	0.65 mm	325	287	264	551
24 mm	0.63 mm	267	225	206	409
	0.64 mm	283	245	220	454
	0.65 mm	301	258	232	506

Simulation results with different striatal-to-background ratio settings for left and right chambers of the phantom for  $^{99m}\text{Tc}$  and  $^{123}\text{I}$  after 45 iterations (LS denotes the left striatal, RS the right striatal, and BG the background).

**Table 2**

	$^{99m}\text{Tc}$				$^{123}\text{I}$			
	LS/BS	RS/BG	LS/BG	RS/BG	LS/BS	RS/BG	LS/BG	RS/BG
Real Ratio	6:1	3:1	10:1	8:1	6:1	3:1	10:1	8:1
Measured Ratio	3.9:1	2.1:1	6.1:1	5.0:1	4.0:1	2.1:1	6.1:1	5.1:1
Recovery Ratio (%)	65.98	71.49	62.48	64.80	64.09	69.85	61.98	63.32
Sections (45 iters)								
								

**Table 3**

Optimum collimator configuration & BiCoreTM collimators specifications.

Isotope	Proposed Energy-optimized Collimator					
	<sup>57</sup> Co	<sup>99m</sup> Tc	<sup>123</sup> I	<sup>111</sup> In	LEHR <sup>99m</sup> Tc	MELP <sup>67</sup> Ga
Hole shape	Square	Square	Square	Square	Hexagonal	Hexagonal
Number of Holes	16384	16384	16384	16384	148000	14000
Hole length	23 mm	23 mm	23 mm	23 mm	24.05 mm	40.64 mm
Septal thickness	0.32 mm	0.32 mm	0.32 mm	0.32 mm	0.16 mm	1.14 mm
Hole material	Tungsten alloy	Tungsten alloy	Tungsten alloy	Tungsten alloy	Lead	Lead
Hole Diameter	1.28 mm	1.28 mm	1.28 mm	1.28 mm	1.11 mm	2.94 mm
Sensitivity @ 10 cm	291 cpm/uCi	261 cpm/uCi	241 cpm/uCi	504 cpm/uCi	202 cpm/uCi	310 cpm/uCi
Resolution @ 10 cm	6.82 mm	6.91 mm	7.08 mm	7.29 mm	7.4 mm	12.5 mm
Septal Penetration	3.7%	4.1%	11.3%	17.9%	1.5%	1.2%

Resolution and sensitivity (@10 cm) comparisons of the optimal energy-optimized collimator with other collimators reported.

**Table 4**

Isotope	Proposed Energy-optimized Collimator				Philips BrightView X & XCT collimators	
	$^{57}\text{Co}$	$^{99m}\text{Tc}$	$^{123}\text{I}$	$^{111}\text{In}$	$^{99m}\text{Tc}$	$^{67}\text{Ga}$
Resolution (mm)	6.82	6.91	7.08	7.29	7.4	10.9
Sensitivity (cpm/uCi)	291	261	241	504	168	212

Isotope	GE Infinia			Zeinali 2012[22]			Philips Precedence SPECT /16MDCT scanner	
	$^{99m}\text{Tc}$	$^{67}\text{Ga}$	250 keV	$^{99m}\text{Tc}$	250 keV	$^{99m}\text{Tc}$	$^{99m}\text{Tc}$	$^{177}\text{Lu}$
Resolution (mm)	7.4	9.4	8.0	8.0	10.3	7.4	7.4	11.3
Sensitivity (cpm/uCi)	160	144	235	235	200	146	146	212